





Brown Carbon Spheres in East Asian Outflow and Their Optical Properties

Duncan T. L. Alexander, *et al. Science* **321**, 833 (2008); DOI: 10.1126/science.1155296

The following resources related to this article are available online at www.sciencemag.org (this information is current as of August 11, 2008):

Updated information and services, including high-resolution figures, can be found in the online version of this article at:

http://www.sciencemag.org/cgi/content/full/321/5890/833

Supporting Online Material can be found at:

http://www.sciencemag.org/cgi/content/full/321/5890/833/DC1

This article appears in the following subject collections:

Atmospheric Science http://www.sciencemag.org/cgi/collection/atmos

Information about obtaining **reprints** of this article or about obtaining **permission to reproduce this article** in whole or in part can be found at:

http://www.sciencemag.org/about/permissions.dtl

On Earth, Fe³⁺ is normally converted to Fe²⁺ in aqueous environments by acidophilic bacteria (19–21). If an Fe^{2+} phase does exist, then a reducing element must have been present at Mawrth Vallis in order to convert the Fe³⁺ to Fe²⁺, or some form of activity [such as hydrothermal processes (22-24)] could have reduced the nontronite or released abundant Fe²⁺ in solution that precipitated out before being converted to Fe3+. Thus, the complex and potentially multi-event formation conditions of phyllosilicates at Mawrth Vallis present a fascinating window into past aqueous activity on Mars.

References and Notes

- 1. J. R. Michalski, E. Z. Noe Dobrea, Geology 35, 951
- 2. S. Murchie et al., J. Geophys. Res. 112, 10.1029/ 2006]E002682 (2007).
- 3. See supporting material on Science Online.
- 4. F. Poulet et al., Nature 438, 623 (2005).
- 5. J.-P. Bibring et al., Science 307, 1576 (2005).

- 6. D. Loizeau et al., J. Geophys. Res. 112, 10.1029/ 2006]E002877 (2007).
- 7. J. F. Mustard et al., Nature, 10.1038/nature07097
- 8. J. L. Bishop, E. Murad, M. D. Dyar, Clay Miner. 37, 617 (2002).
- 9. J. L. Bishop, J. Madejova, P. Komadel, H. Fröschl, Clay Miner. 37, 607 (2002).
- 10. R. E. Milliken et al., Geology, in press.
- 11. J. R. Michalski et al., paper presented at the 7th International Mars Conference, Pasadena, CA, 2007.
- 12. J. J. Wray, B. L. Ehlmann, S. Squyres, J. F. Mustard, R. L. Kirk, Geophys. Res. Lett., 10.1029/2008GL034385
- 13. E. Z. Noe Dobrea et al., paper presented at the Lunar and Planetary Science Conference, Lunar and Planetary Institute, Houston, TX, 2008.
- 14. J. L. Bandfield, V. E. Hamilton, P. R. Christensen, Science 287, 1626 (2000).
- 15. J. L. Bishop, P. Schiffman, M. D. Lane, M. D. Dyar, paper presented at the Lunar and Planetary Science Conference, Lunar and Planetary Institute, Houston, TX,
- 16. J. L. Bishop et al., Clays Clay Miner. 55, 1 (2007).
- 17. H. Chamley, Clay Sedimentology (Springer-Verlag, New York, 1989).

- 18. M. L. Jackson, Clays Clay Miner. 6, 133 (1957).
- 19. H. A. Lowenstam, Science 211, 1126 (1981).
- 20. K. H. Nealson, Annu. Rev. Earth Planet. Sci. 25, 403
- 21. T. D. Brock, J. Gustafson, Appl. Environ. Microbiol. 32, 567 (1976).
- 22. M. J. Nelson, H. E. Newsom, D. S. Draper, Geochim. Cosmochim. Acta 69, 2701 (2005).
- 23. J. W. Stucki, D. Tessier, Clays Clay Miner. 39, 137 (1991).
- 24. P. R. L. Browne, Annu. Rev. Earth Planet. Sci. 6, 229 (1978).
- 25. The authors thank E. Cloutis and an anonymous reviewer for helpful editorial comments and the CRISM Science Team for acquisition of the images. Supported by NASA's Mars Reconnaissance Orbiter project, Mars Data Analysis program, Mars Fundamental Research program, and the NASA Astrobiology Institute.

the wide range of values found in the literature

(3-11), this approach ignores the possibility of rich variations in the refractive indices of carbon

arising from both changes in emission source and changes during transport in the atmosphere. To improve the accuracy of direct forcing models, it

is necessary to have more precise information on the size, shape, composition, mixing state, and

refractive indices of individual carbonaceous aero-

sols. It is difficult to determine these parameters

from light-optical measurements alone because

the signals are averaged over all aerosol compo-

nents (size, composition, structure; see fig. S1).

(TEM) method to identify the optical properties

of individual particles in ambient aerosols. We

applied this method to the highly abundant carbon spheres found in all examined samples of

ambient aerosols collected above the Yellow Sea

during the Asian Pacific Regional Aerosol

Characterization Experiment (ACE-Asia) (12);

bulk optical properties, scanning electron micros-

copy images of samples taken simultaneously

We used a transmission electron microscopy

Supporting Online Material

www.sciencemag.org/cgi/content/full/321/5890/830/DC1 Materials and Methods

Table S1 References Movie S1

28 April 2008: accepted 17 June 2008 10.1126/science.1159699

Brown Carbon Spheres in East Asian Outflow and Their Optical Properties

Duncan T. L. Alexander, Peter A. Crozier, 2* James R. Anderson³

Atmospheric aerosols play a substantial role in climate change through radiative forcing. Combustion-produced carbonaceous particles are the main light-absorbing aerosols; thus, quantifying their optical properties is essential for determining the magnitude of direct forcing. By using the electron energy-loss spectrum in the transmission electron microscope, we quantified the optical properties of individual, submicrometer amorphous carbon spheres that are ubiquitous in East Asian-Pacific outflow. The data indicate that these common spheres are brown, not black, with a mean refractive index of 1.67 - 0.27i (where $i = \sqrt{1}$) at a wavelength of 550 nanometers. The results suggest that brown carbon aerosols should be explicitly included in radiative forcing models.

The importance of the impact of tropospheric aerosols on Earth's radiative balance and the uncertainty associated with radiative forcing due to aerosols are now well established by the large body of research summarized in the reports from the Intergovernmental Panel on Climate Change (1, 2). A substantial fraction of the anthropogenic aerosol mass is in the form of carbonaceous particles arising from fossil fuel and biomass burning. (Carbonaceous aerosols also derive from natural biogenic emissions.) Most direct radiative forcing models classify carbonaceous particles into two main components, consisting of either negligibly absorbing organic carbon or strongly absorbing black carbon (1, 2). Optical properties are incorporated through

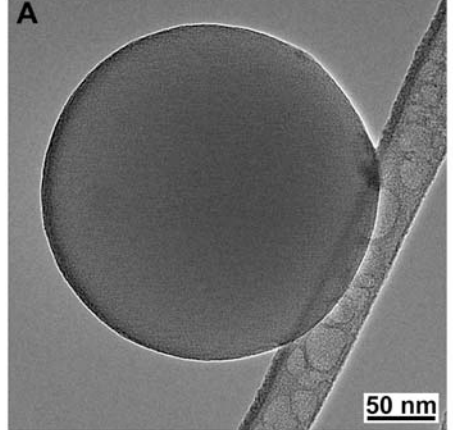
¹LeRoy Evring Center for Solid State Science, Arizona State University, Post Office Box 871704, Tempe, AZ 85287, USA. ²School of Materials, Arizona State University, Post Office Box 878706, Tempe, AZ 85287, USA. 3Department of Mechanical and Aerospace Engineering, Arizona State University, Post

*To whom correspondence should be addressed. E-mail: crozier@asi.edu

Office Box 876106, Tempe, AZ 85287, USA.

the inclusion of model parameters that account mainly for the size distribution and refractive indices of the particles.

Aside from the problem of choosing suitable refractive indices for both forms of carbon from



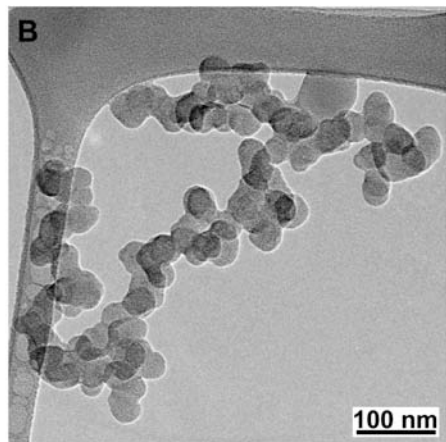


Fig. 1. A bright-field TEM image of a typical amorphous carbon sphere (A) and a soot carbon particle (B) from the atmospheric aerosol sampled at an altitude of 30 m during flight 13 of ACE-Asia.

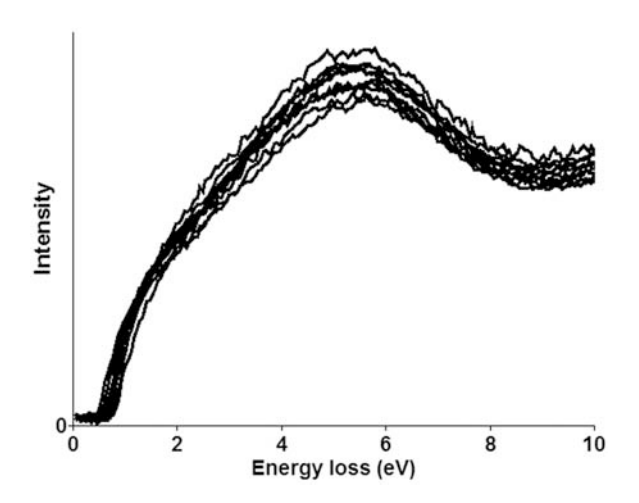
with those described here, and details of flight legs are discussed by Clarke *et al.* (13). The study of the spheres, and their chemical compositions, indicates that they belong to the category of "brown carbon" that has recently become the subject of intense discussion in the atmospheric community (6, 14–16). Uniquely, we were able to specify their full-spectrum optical properties, thus providing greater insight into their impact on direct radiative forcing.

In terms of their morphology and nature, the carbon spheres differ substantially from typical soot carbon. Whereas soot carbon particles consist of aggregates of spherules mostly 20 to 60 nm in diameter, typically with an internal structure of curved graphenelike layers (17-21), and are often internally mixed with other aerosol particles, the carbon spheres are large (e.g., diameters of 100 to 400 nm), amorphous, and predominantly isolated (Fig. 1). As such, they are similar to the "tar balls" described by Pósfai et al. (22), although it is not clear that the carbon spheres in East Asian outflow described here have the same biomassburning origin as tar balls. Further, whereas soot carbon is formed during combustion, within the flame, the carbon spheres are probably formed postcombustion by a gas-phase condensation (22-24). As a result, the spheres are always externally mixed with other carbonaceous combustion products, such as soot. The TEM method used here allows us to determine the optical properties of individual, sub-um spheres within the externally mixed aerosol (24). A similar exactitude of selection is not possible with use of conventional light-optical techniques that average over the mixed aerosol (15). Moreover, whereas light-optical laser measurements are typically made for just one or two wavelengths, our measurements cover the full spectrum of wavelengths from the infrared, through the visible, and into the ultraviolet.

The TEM method uses high spatial resolution electron energy-loss spectroscopy (EELS) to determine the dielectric function, $\varepsilon(E) = \varepsilon_1 + i\varepsilon_2$, for a particle (24), which can then be transformed into refractive indices, $N = n - ik = \sqrt{\epsilon}$, where the energy loss is $E = hc/\lambda$, with Planck's constant h, optical wavelength λ , and speed of light c (25). To determine optical properties in the visible regime of $\lambda = 400$ to 700 nm requires accurate EELS data from energy losses of 1.8 to 3.1 eV, which we obtained with a Tecnai F20 UT TEM (FEI, Hillsboro, Oregon) equipped with a monochromated gun, yielding a spectral resolution of 0.25 eV. The dielectric function was obtained from a Kramers-Kronig transformation of the spectrum (26-28), as described in (24).

Typical low-loss (0 to 10 eV) energy-loss spectra taken from the amorphous carbon spheres are shown in Fig. 2. The spectra are similar in form, indicating that the spheres share similar materials and optical properties. The π^* plasmon at ~6 eV that correlates with sp² hybridization is not the sharp peak seen for soot carbon but rather a broad peak that extends

Fig. 2. Experimentally acquired low-loss spectra from typical carbon spheres (deconvoluted spectra to remove the effects of plural scattering and the zero-loss peak) plotted on linear axes. The scattering intensities of the spectra have also been scaled relative to each other in order to aid comparison. The spectra are all similar in form, partly a consequence of the similarity of their material and their optical properties (24).



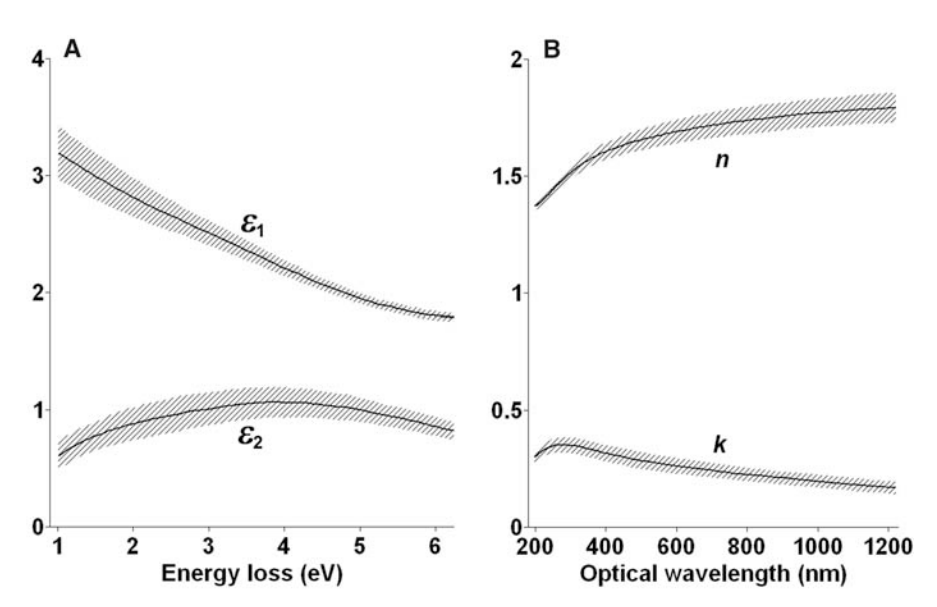
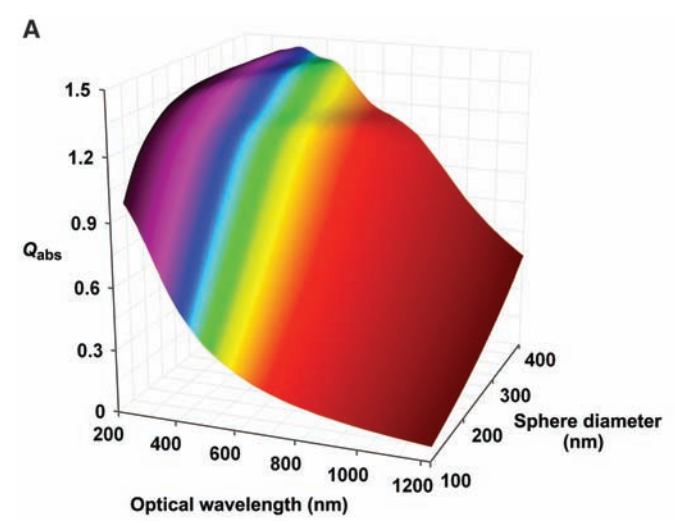


Fig. 3. Mean complex dielectric functions ε_1 and ε_2 against electron energy loss (**A**) and mean refractive indices n and k against optical wavelength (**B**) for 28 analyzed spheres ranging from 130 to 400 nm in diameter (sampled at altitudes of 30 m and 610 m). The shaded bands represent the variance in the mean for the sampling population. The small size of these bands indicates that the spheres have relatively uniform optical properties. k is low in the infrared (>800 nm), increases through the visible, and peaks in the near ultraviolet (<400 nm), thus suggesting that the spheres will appear brown.

down to ~1 eV. Figure 3A shows the energy dependence of the mean dielectric functions of 28 amorphous carbon spheres (sampled from altitudes of 30 m and 610 m), as determined by using the Kramers-Kronig analysis (24). In Fig. 3B, these curves are transformed into mean refractive indices against optical wavelength. For $\lambda = 550$ nm, the mean refractive index is m =1.67 – 0.27i. This conforms to neither the refractive indices of soot carbon [e.g., $m \approx 1.75 - 0.63i$ to 1.95 - 0.79i for void-free soot carbon (4)] nor the refractive indices for negligibly absorbing organic carbon ($m \approx 1.5 - 0i$). It is also separate from that of the humiclike substances, which have recently been receiving attention as a type of brown carbon because their refractive indices indicate substantially lower optical absorption $(m \approx 1.5 - 0.002i)$ (7, 29). Thus, assuming a continuum of carbon species exists (30), the

carbon spheres described here represent a more strongly absorbing carbon compared with the weakly absorbing, soluble, humiclike substances.

In contrast to laser scattering, our approach determines refractive indices from $\lambda \approx 1200 \text{ nm}$ in the infrared, through the visible ($\lambda \sim 400$ to 700 nm), and into the ultraviolet ($\lambda < 400$ nm), as shown in Fig. 3B. In this figure, it can be seen that optical absorption, represented by k, is low in the infrared and visible red; increases through the visible red, yellow, green, and blue; and peaks in the near-ultraviolet. This increase in absorption with decreasing wavelength indicates that the spheres are constituted by a brown form of carbon, thus confirming their nature as different from that of the black soot carbon. Brown carbon as an aerosol component has recently "come into the forefront of atmospheric research" (16). However, its exact nature has remained ill-



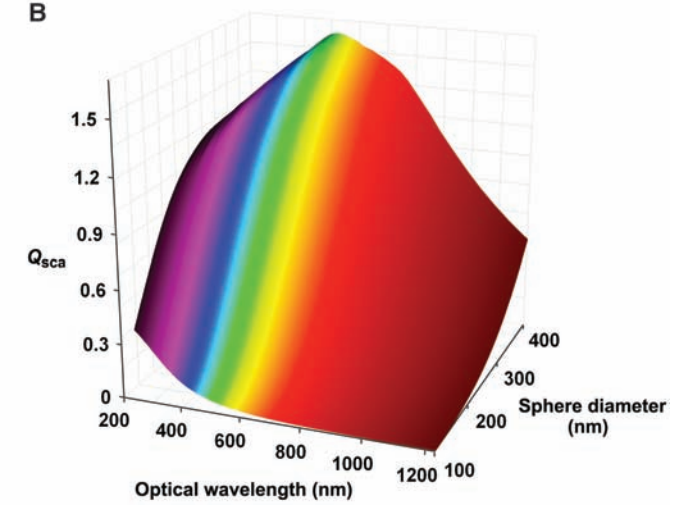


Fig. 4. Diameter and optical wavelength dependence of the light absorbing and scattering efficiencies (25), $Q_{\rm abs}$ (**A**) and $Q_{\rm sca}$ (**B**), of the carbon spheres. The calculations of $Q_{\rm abs}$ and $Q_{\rm sca}$ used the mean refractive indices from Fig. 3B.

The plots are colored to match the colors of the optical wavelengths; darkening of the red at high wavelengths and of the violet at low wavelengths represent infrared and ultraviolet, respectively.

Table 1. Estimated optical and physical properties for typical carbon sphere and soot carbon particles in the samples studied, calculated for $\lambda=550$ nm (apart from \mathring{A}_{abs}). Assumptions used for determining the soot carbon optical properties are given in the main text.

Property	Carbon sphere	Soot carbon
N = n - ik	1.27 - 0.27 <i>i</i>	1.95 - 0.79i
Average spherule diameter (nm)	230	32
Number of spherules	1	55
$\sigma_{abs} (\times 10^{-14} \text{ m}^2)$	4.0	0.8
$\sigma_{sca} (\times 10^{-14} \text{ m}^2)$	3.2	0.2
ω_0	0.44	0.23
ρ (g cm ⁻³)	~1.4-1.6	1.8-2.0
MAE $(m^2 g^{-1})$	~3.6-4.1	4.3-4.8
MSE (m2 g-1)	~3.2-3.7	1.3-1.4
Å _{abs}	~1.5	~1

defined. Our measurements defined the optical properties of a brown carbon species, an essential step toward modeling and accounting for their effects. For instance, by using Mie theory, in Fig. 4 we model the light absorption and scattering efficiencies (Q_{abs} and Q_{sca}) of the spheres against optical wavelength and sphere diameter, where $Q_{\rm abs} = \sigma_{\rm abs}/\pi r^2$ (absorption cross section, $\sigma_{\rm abs}$; sphere radius, r) and analogously $Q_{\text{sca}} = \sigma_{\text{sca}}/\pi r^2$. As sphere diameter rises, the number of contributing scattering modes increases, increasing absorption and modifying the form of the curves of $Q_{\rm abs}$ and $Q_{\rm sca}$ versus λ . The spectral dependence of absorption is parameterized by the Ångström exponent for absorption (Aabs), for which $\sigma_{abs} \propto \lambda^{-A_{abs}}$. From Fig. 4, it can be understood that Aabs will vary depending on sphere diameter. However, for the measured mean diameter of 230 nm of the spheres analyzed here, $A_{abs} \approx$ 1.5 for an optical range of $\lambda = 380$ to 1000 nm,

which is consistent with a brown nature and with values for mixed aerosols (15).

The EELS carbon K-edge intensity has been used to calculate the density of carbon atoms for the optically analyzed carbon spheres, as described in (24). From this, we estimated that their physical densities lie in the range of ~ 1.4 to 1.6 g cm⁻³. By using this together with absorption cross sections that we determined using Mie theory, we estimated a mean mass absorption efficiency (MAE) for the spheres to be \sim 3.6 to 4.1 m² g⁻¹ for λ = 550 nm. This is slightly lower than ACE-Asia measurements indicating that the MAE for the total light-absorbing carbon content was ~7 ± $2 \text{ m}^2 \text{ g}^{-1}$ (13). It is also comparable with estimates of the MAE of soot carbon at $\lambda = 550$ nm (Table 1) (4), such that the contribution to atmospheric light absorption by the spheres may not be readily identified or discriminated from that due to soot by the measurement of MAE performed at a single wavelength.

The amorphous carbon spheres make a contribution to direct radiative forcing that is comparable to that of soot. For the samples analyzed here. the average sphere has a diameter of ~230 nm and a refractive index at $\lambda = 550$ nm of m = 1.67 – 0.27i. A typical carbon soot particle in the samples consists of an aggregate of ~55 spherules of ~32-nm diameter (derived by an analysis of approximate spherule numbers and sizes in TEM images of 50 randomly chosen soot carbon particles; see Fig. 1B for a typical aggregate). Assuming an upper-bound refractive index of m = 1.95 – 0.79i for the soot (4), along with a fractal dimension of 1.8 and a fractal prefactor of 8 (17), we calculated absorption cross sections, σ_{abs} , by using Mie theory (25) for the spheres and Rayleigh-Debye-Gans theory (31) for the soot. The absorption cross section of a typical sphere is almost a factor of 5 greater than that for a typical soot aggregate, that is, $\sigma_{abs} \approx 3.9 \times 10^{-14} \text{ m}^2$ (sphere) versus $\sigma_{abs} \approx 0.82 \times 10^{-14} \text{ m}^2$ (soot).

Other optical and physical properties are compared in Table 1.

Thus, on a particle-by-particle basis, the carbon spheres show light absorption commensurate to, or greater than, that of the soot particles conventionally accepted as being the dominant form of light-absorbing carbon. Our statistical measurements also find that the carbon spheres are very abundant. Specifically, for the nominal particle size range of 0.3 to 2.0 µm studied in these samples, the number ratios of sphere:soot particles is ~1:1 for the specimen sampled at 30 m altitude and ~3:1 for the specimen sampled at 610 m. Moreover, similar carbon spheres have been found abundant or dominant in other regions, such as central Europe and South Africa (22), and in urban aerosols in areas such as Phoenix. There may be other ways in which the unique optical properties of the carbon spheres may affect radiative force relative to soot. For instance, owing to their reduced absorption of infrared compared with visible, their role in absorption of reradiated heat will be quite different to that for black soot.

Taking account of both the abundance of spheres and their optical properties, these measurements challenge the usual supposition in radiative forcing calculations of atmospheric carbon being either negligibly absorbing organic carbon or strongly absorbing black soot carbon. For modeling of radiative forcing from aerosols to be accurate, scattering and absorption by brown carbon needs to be explicitly included.

References and Notes

- V. Ramaswamy et al., in Climate Change 2001: The Scientific Basis, J. Houghton et al., Eds. (Cambridge Univ. Press, Cambridge, 2001), pp. 349–416.
- P. Forster et al., Changes in Atmospheric Constituents and in Radiative Forcing, http://ipcc-wg1.ucar.edu/wg1/ wa1-report.html (2007).
- 3. R. C. Millikan, J. Opt. Soc. Am. 51, 698 (1961).
- T. C. Bond, R. W. Bergstrom, Aerosol Sci. Technol. 40, 27 (2006).
- 5. E. Dinar et al., Faraday Discuss. 137, 279 (2008).

- T. W. Kirchstetter, T. Novakov, P. V. Hobbs, J. Geophys. Res. 109, D21208 (2004).
- 7. A. Hoffer *et al.*, *Atmos. Chem. Phys.* **6**, 3563 (2006).
- 8. H. Horvath, Atmos. Environ. 27A, 293 (1993).
- 9. J. T. McCartney, S. Ergun, Fuel 37, 272 (1958).
- A. B. Pluchino, S. S. Goldberg, J. M. Dowling,
 C. M. Randall, Appl. Opt. 19, 3370 (1980).
- 11. J. L. Hand et al., J. Geophys. Res. 110, D21210 (2005).
- 12. B. J. Huebert *et al.*, *J. Geophys. Res.* **108**, 8633 (2003).
- 13. A. D. Clarke *et al.*, *J. Geophys. Res.* **109**, D15S09 (2004).
- 14. M. O. Andreae, A. Gelencsér, *Atmos. Chem. Phys.* **6**, 3131 (2006)
- 15. R. W. Bergstrom *et al.*, *Atmos. Chem. Phys.* **7**, 5937
- (2007). 16. H. Lukacs *et al.*, *J. Geophys. Res.* **112**, D23S18 (2007).
- 17. G. M. Faeth, Ü. Köylü, *Combust. Sci. Tech.* **108**, 207 (1995)
- D. M. Roessler, F. R. Faxvog, R. Stevenson, G. W. Smith, in *Particulate Carbon*, D. Siegla, G. Smith, Eds. (Plenum, New York, 1981), pp. 57–89.

- R. L. Vander Wal, A. J. Tomasek, Combust. Flame 136, 129 (2004).
- 20. L. H. van Poppel *et al.*, *Geophys. Res. Lett.* **32**, L24811
- Y. Chen, N. Shah, A. Braun, F. E. Huggins, G. P. Huffman, *Energy Fuels* 19, 1644 (2005).
- 22. M. Pósfai et al., J. Geophys. Res. 109, D06213 (2004).
- J. Hallet, J. G. Hudson, C. F. Rogers, *Aerosol Sci. Technol.* 10, 70 (1989).
- Materials and methods are available as supporting material on *Science* Online.
- C. Bohren, D. Huffman, Absorption and Scattering of Light by Small Particles (Wiley, New York, 1983).
- 26. R. H. Ritchie, Phys. Rev. 106, 874 (1957).
- 27. H. Raether, Surf. Sci. 8, 233 (1967).
- 28. R. F. Egerton, Electron Energy-Loss Spectroscopy in the Electron Microscope (Plenum, New York, ed. 2, 1996).
- N. Havers, P. Burba, J. Lambert, D. Klockow, J. Atmos. Chem. 29, 45 (1998).
- H. Sun, L. Bierdermann, T. C. Bond, Geophys. Res. Lett. 34, L17813 (2007).

- 31. C. M. Sorensen, Aerosol Sci. Technol. 35, 648 (2001).
- 32. This material is based upon work supported by NASA under grant no. NNG04GB37G issued through the Radiation Sciences Program. Participation in ACE-Asia was funded by NSF grant ATM-0002513. The authors acknowledge support of the National Center for Electron Microscopy (NCEM), Lawrence Berkeley Laboratory, which is supported by the U.S. Department of Energy under contract no DE-AC02-05CH11231. We respectfully acknowledge technical support from the late C. Nelson of the NCEM.

Supporting Online Material

www.sciencemag.org/cgi/content/full/321/5890/833/DC1 Materials and Methods Figs. S1 to S3 References

16 January 2008; accepted 2 July 2008 10.1126/science.1155296

A Conserved Mutation in an Ethylene Biosynthesis Enzyme Leads to Andromonoecy in Melons

Adnane Boualem, Mohamed Fergany, Ronan Fernandez, Christelle Troadec, Antoine Martin, Halima Morin, Marie-Agnes Sari, Fabrice Collin, Jonathan M. Flowers, Michel Pitrat, Michael D. Purugganan, Catherine Dogimont, Abdelhafid Bendahmane

Andromonoecy is a widespread sexual system in angiosperms characterized by plants carrying both male and bisexual flowers. In melon, this sexual form is controlled by the identity of the alleles at the *andromonoecious* (a) locus. Cloning of the a gene reveals that andromonoecy results from a mutation in the active site of 1-aminocyclopropane-1-carboxylic acid synthase. Expression of the active enzyme inhibits the development of the male organs and is not required for carpel development. A causal single-nucleotide polymorphism associated with andromonoecy was identified, which suggests that the a allele has been under recent positive selection and may be linked to the evolution of this sexual system.

ost angiosperms have hermaphroditic flowers containing both male and female organs; nevertheless, sex determination can result in the formation of separate male and female flowers on either the same (monoecy) or different individuals (dioecy). Andromonoecy, where plants carry both male and perfect bisexual flowers, has evolved independently numerous times (1) and is found in ~4000 species in 33 angiosperm families (2). Several species in the Cucurbitaceae, including cucumber (*Cucumis sativus*)

¹INRA (Institut National de la Recherche Agronomique)—CNRS, UMR1165, Unité de Recherche en Génomique Végétale, 2 rue Gaston Crémieux, F-91057 Evry, France. ²INRA, UR501, Laboratoire de Biologie Cellulaire, Institut Jean Pierre Bourgin, F-78026 Versailles, France. ³CNRS, UMR 8601, Laboratoire de Chimie et Biochimie Pharmacologiques et Toxicologiques, Université René Descartes, 45 Rue des Saint-Pères, F-75270 Paris Cedex 06, France. ⁴Department of Biology, Center for Genomics and University, New York, NY 10003, USA. ⁵INRA, UR 1052, Unité de Génétique et d'Amélioration des Fruits et Légumes, BP 94, F-84143 Montfavet, France.

*To whom correspondence should be addressed. E-mail: bendahm@evry.inra.fr

and melon (Cucumis melo), have bisexual floral primordia, but often have flowers limited to a single sex. Sex determination occurs by the selective arrest of either the male stamen or female carpel during development (3, 4). In melon, sex determination is governed by the genes andromonoecious (a) and gynoecious (g), and the interplay of these two genes results in a range of sexual types (5, 6). Monoecious (A-G-) and andromonoecious (aaG-) individuals bear male flowers on the main stem and, respectively, female or hermaphrodite flowers on axillary branches, whereas gynoecious (AAgg) and hermaphrodite (aagg) individuals only bear female and hermaphrodite flowers, respectively (6). In addition, cucurbit sex expression patterns can be modified by hormones, such as ethylene, and by environmental factors (7, 8).

In *C. melo*, most plants are monoecious or andromonoecious because of the *a* locus, which has been mapped to a genetic interval of 25.2-centimorgans (9). We cloned the *a* locus by constructing high-resolution genetic and physical maps (fig. S1A), used chromosome walking to construct a bacterial artificial chromosome (BAC)

contig anchored to the genetic map (fig. S1A), delimited the a locus to a single BAC clone, and revealed seven candidate genes within 107 kilobase pairs (kbp) (fig. S1B) (10). The a locus flanking marker sequences L41 and R5 were used to identify a 14-kbp region containing a gene encoding for a 1-aminocyclopropane-1-carboxylic acid synthase (ACS), designated CmACS-7 on the basis of homology to the Arabidopsis ACS-7 gene (At4g26200). ACS is a pyridoxal 5'-phosphate (PLP)-dependent enzyme that catalyzes the first committed, and generally rate-limiting, step in the production of 1-aminocyclopropane-1-carboxylic acid (ACC) from S-adenosylmethionine (SAM) in ethylene biosynthesis in higher plants (11). Ethylene is then made from ACC by the enzyme ACC oxidase.

A TILLING (targeting induced local lesions in genomes) approach confirmed the role of CmACS-7 in sex determination (12). We identified six mutations in the full CmACS-7 gene; four silent or intronic and two that led to missense mutations at G19E and D376N (13). The G19E change occurs in a highly conserved amino acid position and may affect the function of the protein (14), whereas the D376N modification affects a nonconserved amino acid position (Fig. 1A). Backcrosses to the wild type showed that, for more than 100 F₂ plants for each cross, that the D376N mutation, as well as the silent and intronic mutations, had no sexual phenotype (Fig. 1B and fig. S2). In contrast, plants homozygous for the G19E mutation were andromonoecious (Fig. 1B and fig. S2). On the basis of these data, we concluded that CmACS-7 is the andromonoecious gene.

A 14-kbp genomic sequence of melon accessions PI124112 and Védrantais was used to map single-nucleotide polymorphisms (SNPs) linked to *CmACS-7*. The minimal interval between allelic variants was localized to a 2438-bp DNA fragment containing 560 bp of the proximal promoter, as well as exons 1 and 2 and a part of exon 3 (fig. S1C). We identified no differences linked to sex phenotype in the proximal promoter sequence and quantitative reverse transcription polymerase chain reaction (RT-PCR) detected no significant